

Efficient Topological Layer based on Persistent Landscapes

Kwangho Kim ^{*1}, Jisu Kim ^{†2}, Joon Sik Kim¹,
Frédéric Chazal², and Larry Wasserman¹

¹Carnegie Mellon University, USA

²Inria Saclay, France

05 February, 2020

Abstract

We propose a novel topological layer for general deep learning models based on persistent landscapes, in which we can efficiently exploit underlying topological features of the input data structure. We use the robust DTM function and show differentiability with respect to layer inputs, for a general persistent homology with arbitrary filtration. Thus, our proposed layer can be placed anywhere in the network architecture and feed critical information on the topological features of input data into subsequent layers to improve the learnability of the networks toward a given task. A task-optimal structure of the topological layer is learned during training via backpropagation, without requiring any input featurization or data preprocessing. We provide a tight stability theorem, and show that the proposed layer is robust towards noise and outliers. We demonstrate the effectiveness of our approach by classification experiments on various datasets.

Keywords: topological data analysis, deep learning, persistent diagram, persistent homology, topological feature, stability theorem

*kwanghk@cmu.edu

†jisu.kim@inria.fr

1 Introduction

With its strong generability, deep learning has become one of the most pervasively applied techniques in machine learning. However, there is still no general principle toward an optimal model architecture for a given task and the performance often varies drastically from task to task. To improve learnability of deep learning models, various architectures and layer structures have been proposed. Some people scheme out an efficient data processing method through specialized feature maps. For instance, it is widely known that inserting a convolutional layer greatly improves visual object recognition and other tasks in computer vision (e.g., Krizhevsky et al., 2012; LeCun et al., 2016). On the other hand, a large body of work in computer vision focuses on choosing optimal initial architectures (He et al., 2016; Simonyan & Zisserman, 2014; Szegedy et al., 2015). Moreover, a substantial amount of recent studies have explored how various properties of neural networks (e.g., the depth, width, and connectivity) relate to their expressivity and generalization capability (e.g., Daniely et al., 2016; Guss & Salakhutdinov, 2018; Raghu et al., 2017).

In this paper, we explore an alternative way to enhance learnability of deep learning models by introducing a novel *topological layer* which feeds topological features of underlying data structure in an arbitrary network. The power of topology lies in its capacity which differentiates sets in topological space in a robust and meaningful geometric way Carlsson (2009); Ghrist (2008). It provides important insight to the global "shape" of data structure via *persistent homology* Zomorodian & Carlsson (2005). The use of topological methods in data analysis has been limited by the difficulty of combining the main tool of the subject, persistent homology, with statistics and machine learning. However, a series of recent studies have reported a notable success on utilizing topological methods in data analysis (e.g., Brown & Knudson, 2009; Emrani et al., 2014; Gamble & Heo, 2010; Liu et al., 2016; Nanda & Sazdanović, 2014; Pereira & de Mello, 2015; Seversky et al., 2016; Tralie & Perea, 2018; Umeda, 2017; Venkataraman et al., 2016; Zhu, 2013)

Specifically, we design a novel topological layer that can be placed into any deep learning model based on tools in topological data analysis. The proposed topological layer consists of many structure elements, each of which is a differentiable parametrized projection and to be trained in the way that it can pass critical information on the topological feature of layer's input through the network in order to improve the task-specific learning performance. There are at least three benefits of using the topological layer in deep learning; 1) we can efficiently extract robust global features of input data that otherwise would not be readily accessible via traditional feature maps, 2) the optimal structure of the layer for a given learning task can be easily embodied via backpropagation during training, and 3) with proper filtration it can be applied to arbitrarily complicated data structure even without any data preprocessing.

Related Work. Idea of incorporating topological theories into deep learning has been

explored only recently, but mostly via feature engineering methods where we use some fixed, predefined features that contain topological information (e.g., Liu et al., 2016; Umeda, 2017). Guss & Salakhutdinov (2018); Rieck et al. (2018) proposed a complexity measure for neural network architectures based on topological data analysis. Carlsson & Gabrielsson (2018) applied topological approaches to deep convolutional networks to understand and improve the computations of the network. Hofer et al. (2017) first developed a technique to input persistent diagrams into neural networks by introducing the topological layer. Carrière et al. (2019); Gabrielsson et al. (2019); Hofer et al. (2019); Poulenard et al. (2018) also proposed topology loss function and topology layer in a particular form. Nevertheless, all the previous approaches for topological layer/loss suffer from the following limitations: 1) they rely on a particular parametrized map or filtration, 2) they lack stability result or the result is limited to a particular type of input data representation, and 3) most importantly, the differentiability of persistence homology is not guaranteed for arbitrary input setting therefore we are not guaranteed to use the layer in the middle of deep networks in general.

Contribution. This paper presents a new topological layer that does not suffer from the above limitations. Our topological layer does not rely on particular filtration or parametrized mapping but still possesses favorable theoretical properties. The proposed layer is designed based on weighted persistent landscapes in the way that we suffer less from the extreme persistence distortion. We verify that our stability bound can be tighter than Hofer et al. (2017), and that it is also stable with respect to a small perturbation/noise/outliers in our input data. Importantly, we show that our layer is differentiable with respect to the layer input for a general persistent homology with any valid filtration, so we can place it anywhere in the network to extract topological features where they might be useful.

2 Background and definitions

Topological data analysis (TDA) is a recent and emerging field of data science that relies on topological and geometric tools to infer relevant features for possibly complex data Carlsson (2009). In this section, we briefly review basic concepts and main tools in TDA which we will use to develop our own topological layer. We refer the interested readers reader to Chazal & Michel (2017); Chazal et al. (2009, 2016b); Edelsbrunner & Harer (2010); Hatcher (2002) for further details and formal definitions.

Throughout, we will let \mathbb{X} denotes a subset of \mathbb{R}^d , and X denotes a finite collection of points from an arbitrary space \mathbb{X} , and let $B_x(r)$ denote the open ball centered at x with radius r .

2.1 Simplicial complex, persistent homology, and diagrams

When inferring topological properties of \mathbb{X} from its finite collection of samples X , we rely on *simplicial complex* K , a discrete structure built over the observed points to provide a

topological approximation of the underlying space. Two common examples are the Čech complex and the Vietoris-Rips complex. The *Čech complex* is the simplicial complex where k -simplices correspond to the nonempty intersection of $k + 1$ balls centered at vertices. The *Vietoris-Rips complex*, also referred to as *Rips complex*, is the simplicial complex where simplexes are built based on pairwise distances among its vertices. We refer to Section A for formal definitions.

A collection of simplicial complexes $\mathcal{F} = \{K_a \subset K : a \in \mathbb{R}\}$ satisfying $K_a \subset K_b$ whenever $a \leq b$ is called a *filtration* of K . A typical way of setting the filtration is through a monotonic function on the simplex. A function $f : K \rightarrow \mathbb{R}$ is monotonic if $f(\varsigma) \leq f(\tau)$ whenever ς is a face of τ . Now we let $K_a := f^{-1}(-\infty, a]$, then the monotonicity implies that K_a is a subcomplex of K and $K_a \subset K_b$ whenever $a \leq b$. In this paper, we assume that the filtration is built from a monotonic function.

Persistent homology (Barannikov, 1994; Chazal et al., 2014a; Edelsbrunner et al., 2000; Zomorodian & Carlsson, 2005) is a multiscale approach to represent topological features of the complex K . Specifically, one can apply homology in some degree (e.g., 0-dimension: connected components, 1-dimension: loops, 2-dimension: cavities, ...) with coefficients in some field to the above finite filtered complex, again to obtain a sequence of vector spaces and linear maps such that

$$\mathcal{H}(K_0) \rightarrow \mathcal{H}(K_1) \rightarrow \dots \rightarrow \mathcal{H}(K_n)$$

which we call a *persistence module*. It turns out that the persistence module can be completely described by a finite sequence of pairs $\{(b_i, d_i)\}$ with $b_i < d_i$. For such pair $p_i = (b_i, d_i)$, there is a choice of a nonzero homology class $\alpha_i \in \mathcal{H}(K_{b_i})$ that is not in the image of $\{\mathcal{H}(K_j)\}_{j < b_i}$ and whose image is nonzero in $\mathcal{H}(K_{d_i-1})$ but is zero in $\{\mathcal{H}(K_j)\}_{j \geq d_i}$. We often say α_i is born at b_i and dies at d_i , and will refer to each p_i as *birth-death pair*. In this sense, we call $d_i - b_i$ the persistence of a homological feature (or homological persistence, collectively). Note that for now we have $b_i, d_i \in \{0, 1, \dots, n\}$ but we can generalize to $b_i, d_i \in \mathbb{R}$ by associating to a corresponding increasing sequence of real numbers in the filtration. Finally, considering these pairs as points in the plane, one obtains the *persistence diagram* as below.

Definition 2.1. Let $\mathbb{R}_*^2 := \{(b, d) \in \mathbb{R}^2 : d > b\}$. A *persistent diagram* \mathcal{D} is a finite multiset of $\{p : p \in \mathbb{R}_*^2\}$. We let \mathbb{D} denote the set of all such \mathcal{D} 's.

We will often write $\mathcal{D}_X, \mathcal{D}_{\mathbb{X}}$ to indicate that persistent diagrams are drawn from the simplicial complex constructed on original data source X, \mathbb{X} . In computational settings, there are always only finitely many points with finite numbers in the persistence diagram and we usually truncate d_i 's that persist until the maximum filtration value at that value. Thus, as in Bubenik (2018) we make the following assumption.

Assumption A1. *Throughout this paper, we will only consider persistence diagram space \mathbb{D} where every persistent diagram $\mathcal{D} \in \mathbb{D}$ consists of finitely many points (b, d) with $-\infty < b < d < \infty$.*

Lastly, we define the following metrics to measure the distance between two persistent diagrams.

Definition 2.2 (Bottleneck and Wasserstein distance). *Given two persistence diagrams \mathcal{D}_X and \mathcal{D}_Y , their bottleneck distance (d_B) and q -th Wasserstein distance (W_q) are defined as*

$$d_B(\mathcal{D}_X, \mathcal{D}_Y) = \inf_{\gamma \in \Gamma} \sup_{p \in \mathcal{D}_X} \|p - \gamma(p)\|_\infty,$$

$$W_q(\mathcal{D}_X, \mathcal{D}_Y) = \left[\inf_{\gamma \in \Gamma} \sum_{p \in \mathcal{D}_X} \|p - \gamma(p)\|_\infty^q \right]^{\frac{1}{q}},$$

respectively, where $\|\cdot\|_\infty$ is the usual L_∞ -norm and the set Γ consists of all the bijections $\gamma : \mathcal{D}_X \cup \text{Diag} \rightarrow \mathcal{D}_Y \cup \text{Diag}$, where Diag is the diagonal $\{(x, x) : x \in \mathbb{R}\} \subset \mathbb{R}^2$ with infinite multiplicity.

Note that for $\forall q < \infty$, $d_B(\mathcal{D}_X, \mathcal{D}_Y) \leq W_q(\mathcal{D}_X, \mathcal{D}_Y)$ for any given $\mathcal{D}_X, \mathcal{D}_Y$. As q tends to infinity, the Wasserstein distance approaches the bottleneck distance.

2.2 Persistent Landscapes

A persistence diagram is a multiset, which makes it difficult to analyze and feed as input to learning or statistical methods. Hence, it is useful to transform the persistent homology into a functional Hilbert space, where the analysis is easier and learning methods can be directly applied. Good examples include persistent landscapes (Bubenik, 2015, 2018; Bubenik & Dłotko, 2017) and silhouettes (Chazal et al., 2014b, 2015), both of which are real-valued functions that further summarize the crucial information contained in a persistence diagram. Here we briefly introduce the persistent landscapes as we use them to design our layer.

Landscapes. Let \mathcal{D} denote a persistent diagram that contains N off-diagonal birth-death pairs $\{(b_j, d_j)\}_{j=1}^N$. We first define a set of functions $t \in \mathbb{R}_{+0} \mapsto \Lambda_p(t)$ for each birth-death pair $p = (b, d)$ in \mathcal{D} as follows:

$$\Lambda_p(t) = \begin{cases} t - b, & t \in [b, \frac{b+d}{2}] \\ d - t, & t \in (\frac{b+d}{2}, d] \\ 0, & \text{otherwise} \end{cases} \quad (1)$$

For each birth-death pair p , $\Lambda_p(\cdot)$ is piecewise linear. Then the *persistence landscape* λ of

the persistent diagram \mathcal{D} is defined by the sequence of functions $\{\lambda_k\}_{k \in \mathbb{N}}$, where

$$\lambda_k(t) = kmax_p \Lambda_p(t), \quad t \in [0, T], k \in \mathbb{N}, \quad (2)$$

and $kmax$ is the k -th largest value in the set. Hence, the persistence landscape is a function $\lambda : \mathbb{N} \times \mathbb{R} \rightarrow [0, T]$. T is large enough to satisfy $T > d_{max}$. λ_k is commonly denoted by k -th order persistent landscape.

Note that landscape functions can be evaluated over \mathbb{R} , and are easy to compute. Many recent studies including previously listed ones have revealed that this kind of functional summaries of the persistence module not only show favorable theoretical properties, but can be easily averaged and used for subsequent statistics and machine learning modeling Bubenik (2018); Bubenik & Dłotko (2017); Chazal et al. (2014b).

2.3 Distance to measure (DTM) function

The Distance to measure (DTM) (Chazal et al., 2011, 2016a) is a robustified version of the distance function. More precisely, the DTM $d_{\mu, m_0} : \mathbb{R}^d \rightarrow \mathbb{R}$ for a probability distribution μ with parameter $m_0 \in [0, 1]$ and $r \geq 1$ is defined as

$$d_{\mu, m_0}(x) = \left(\frac{1}{m_0} \int_0^{m_0} (\delta_{\mu, m}(x))^r dm \right)^{1/r},$$

where $\delta_{\mu, m}(x) = \inf\{t > 0 : \mu(\mathbb{B}(x, t)) > m\}$. If r is not specified, then $r = 2$ is used as a default. When μ is a weighted empirical measure $P_n(x) = \frac{1}{n} \sum_{i=1}^n \varpi_i I(X_i = x)$, where I is an indicator function, the empirical DTM is

$$\begin{aligned} \hat{d}_{m_0}(x) &= d_{P_n, m_0}(x) \\ &= \left(\frac{\sum_{X_i \in N_k(x)} \varpi'_i \|X_i - x\|^r}{m_0 \sum_{i=1}^n \varpi_i} \right)^{1/r}, \end{aligned} \quad (3)$$

where $N_k(x)$ is the subset of $\{X_1, \dots, X_n\}$ containing the k nearest neighbors of x , k is such that $\sum_{X_j \in N_{k-1}(x)} \varpi_j < m_0 \sum_{i=1}^n \varpi_i \leq \sum_{X_j \in N_k(x)} \varpi_j$, and $\varpi'_i = \sum_{X_j \in N_k(x)} \varpi_j - m_0 \sum_{j=1}^n \varpi_j$ for one of X_i 's that is k -th nearest neighbor of x and $\varpi'_i = \varpi_i$ otherwise. Hence the empirical DTM behaves similarly to the k -nearest distance with $k = \lfloor m_0 n \rfloor$. The DTM is a preferred choice for the filtration function, since the persistence diagram computed on the DTM is less prone to noise.

3 A novel topological layer based on weighted persistent landscapes

In this section, we present a detailed algorithm to obtain the novel topological layer for a neural network. Let X , \mathcal{D}_X , h_{top} denote input, persistent diagram induced from X , the topological layer, respectively. Broadly speaking, the construction of our topological layer consists of two steps: computing persistent diagram from the input and constructing topological layer from the persistent diagram.

3.1 Computation of diagram: $X \rightarrow \mathcal{D}_X$

For computing the persistence diagram from the input data, we first need to define the filtration. Given a simplicial complex K and a function $f : K \rightarrow \mathbb{R}$, we use the filtration $\mathcal{F} = \{f^{-1}(-\infty, a] \subset K : a \in \mathbb{R}\}$. There can be several choices for the simplicial complex K and the function f . One popular choice for the simplicial complex is the Rips complex, where the complex $K = 2^X$ is the power set of X and the function f is $f(\varsigma) = \frac{1}{2} \max\{d(x_i, x_j) : x_i, x_j \in \varsigma\}$. Another option is when X is a grid (so that there is a natural cubical complex K) and the function f is defined on X , to extend the function to the complex K by $f(\varsigma) = \max\{f(x_i) : x_i \in \varsigma\}$. Then, we compute the persistence diagram of the filtration \mathcal{F} and denote this by \mathcal{D}_X .

One appealing choice for f is the distance to measure (DTM) function (see Section 2.3). As the resultant persistent diagrams from the DTM function are robust to noise (Chazal et al., 2011, 2017), the DTM function has been widely used in topological data analysis Anai et al. (2019); Xu et al. (2019). Nonetheless, despite this and other favorable properties, to best of our knowledge, the DTM function has not been adopted by previous studies in deep learning.

We detail two possible scenarios, where the input data X can be used as either the data points or the weights. First, the input data X is considered as the empirical data points, and then the empirical DTM in (3) with weights ϖ_i 's becomes

$$\hat{d}_{m_0}(x) = \left(\frac{\sum_{X_i \in N_k(x)} \varpi'_i \|X_i - x\|^r}{m_0 \sum_{i=1}^n \varpi_i} \right)^{1/r}, \quad (4)$$

where k and ϖ'_i are determined as in (3).

Second, the input data X is considered as the weights corresponding to fixed points $\{Y_1, \dots, Y_n\}$, and then the empirical DTM in (3) with data points Y_i 's and weights X_i 's becomes

$$\hat{d}_{m_0}(x) = \left(\frac{\sum_{X_i \in N_k(x)} X'_i \|Y_i - x\|^r}{m_0 \sum_{i=1}^n X_i} \right)^{1/r}, \quad (5)$$

where k and ϖ'_i are determined as in (3).

3.2 Construction of topological layer: $\mathcal{D}_X \rightarrow h_{top}$

Our topological layer is defined upon a parametrized mapping which takes any persistent diagram \mathcal{D} to be projected onto \mathbb{R} . Our construction is no longer afflicted by the artificial bending due to separate logarithmic transformations (Hofer et al., 2017), yet still guarantees the crucial information in the persistence diagram to be well preserved by harnessing persistent landscapes (2) with more favorable theoretical properties which we will address in Section 5. Furthermore, insignificant points with low persistence are likely to be ignored systematically without introducing additional nuisance parameters (Bubenik & Dłotko, 2017).

Let \mathbb{R}^{+0} denote $[0, \infty)$. Given a persistent diagram $\mathcal{D} \in \mathbb{D}$ of a certain homological dimension, we compute k -th order persistent landscape function $\lambda_k(t)$ on the fixed interval $t \in [0, T]$ for every $k = 1, \dots, K_{max}$. Then, we compute the weighted average $\bar{\lambda}_\omega(t) := \sum_{k=1}^{K_{max}} \omega_k \lambda_k(t)$ with a weight parameter $\omega = \{\omega_k\}_k$, $\omega_k > 0$, $\sum_k \omega_k = 1$ for all k . Next, we set a resolution $\nu := T/m$, and sample m equal-interval points from $[0, T]$ to obtain $\bar{\Lambda}_\omega = (\bar{\lambda}_\omega(\nu), \bar{\lambda}_\omega(2\nu), \dots, \bar{\lambda}_\omega(m\nu))^\top \in (\mathbb{R}^{+0})^m$. Consequently, we have defined a mapping $\bar{\Lambda}_\omega : \mathbb{D} \rightarrow (\mathbb{R}^{+0})^m$ which is a (vectorized) finite-sample approximation of the weighted persistent landscapes at the resolution ν , at fixed, predetermined locations. Finally, we consider a parametrized differentiable map $g_\theta : (\mathbb{R}^{+0})^m \rightarrow \mathbb{R}$ which takes $\bar{\Lambda}_\omega$ and is differentiable with respect to θ as well. Now, the projection of \mathcal{D} with respect to the mapping $S_{\theta, \omega} := g_\theta \circ \bar{\Lambda}_\omega$ defines a single *structure element* for our topological input layer. We summarize the procedure in Algorithm 1.

Algorithm 1 Structure element for the proposed topological layer from persistent diagram

Input: Persistent diagram $\mathcal{D} \in \mathbb{D}$

1. compute $\lambda_k(t)$ (2) on $t \in [0, T]$ for every $k = 1, \dots, K_{max}$
2. compute the weighted average $\bar{\lambda}_\omega(t) := \sum_{k=1}^{K_{max}} \omega_k \lambda_k(t)$, $\omega_k > 0$, $\sum_k \omega_k = 1$
3. set a resolution $\nu := \frac{T}{m}$, and compute $\bar{\Lambda}_\omega = (\bar{\lambda}_\omega(\nu), \bar{\lambda}_\omega(2\nu), \dots, \bar{\lambda}_\omega(m\nu))^\top \in \mathbb{R}^m$
4. for a parametrized differentiable map $g_\theta : \mathbb{R}^m \rightarrow \mathbb{R}$, define $S_{\theta, \omega} = g_\theta \circ \bar{\Lambda}_\omega$

Output: $S_{\theta, \omega} : \mathbb{D} \rightarrow \mathbb{R}$

The projection $S_{\theta, \omega}$ is continuous at every $t \in [0, T]$. Also note that it is differentiable with respect to ω and θ , regardless of resolution level ν . In what follows, we delineate some guidelines for encoding each parameter.

ω : The weight parameter ω can be initialized as equal weight, i.e. $\omega_k = 1/K_{max} \forall k$, and will be re-determined in the way that a certain landscape that conveys significant information

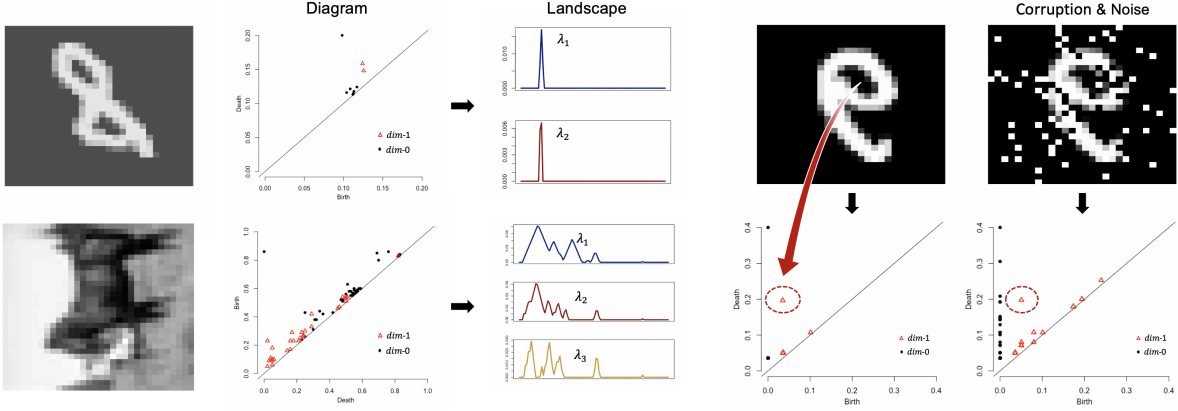


Figure 1: Topological features coded in persistent landscapes for MNIST and CIFAR-10 examples. In the MNIST example, two loops (1-dimensional feature) in ‘8’ are identified and encoded into the 1st and 2nd order landscapes. The CIFAR-10 example shows more involved patterns.

Figure 2: The significant points in the persistent diagram remain almost unchanged even after the corruption and noise processing.

has more weight. In general, lower-order landscapes tend to be more significant than higher-order landscapes (mostly low persistence), but the optimal weights may vary from task to task and thus should be determined after the training process. We use the softmax layer and treat ω_j as j -th entry of the softmax output.

$\theta, \mathbf{g}_\theta$: Likewise, some birth-death pairs p 's, encoded as Λ_p 's in (1), may contain more crucial information about topological features of the input data structure than others. Roughly speaking, this is equivalent to say certain mountains (or their ridge or valley) in the landscape are especially important. Hence, the parametrized map \mathbf{g}_θ should be able to reflect this by its design. In general, it can be done by affine transformation with scale and translation parameter, followed by an extra nonlinearity and normalization if necessary. We list two possible choices as below.

- Affine transformation: with scale and translation parameter $\sigma_i, \mu_i \in \mathbb{R}^m$, $\mathbf{g}_{\theta_i}(\bar{\Lambda}_\omega) = \sigma_i^\top (\bar{\Lambda}_\omega - \mu_i)$ and $\theta_i = (\sigma_i, \mu_i)$.
- Logarithmic transformation: with same $\theta_i = (\sigma_i, \mu_i)$, $\mathbf{g}_{\theta_i}(\bar{\Lambda}_\omega) = \exp(-\sigma_i \|\bar{\Lambda}_\omega - \mu_i\|_2)$.

Note that other constructions of $\mathbf{g}_\theta, \theta, \omega$ are also possible so long as they satisfy the sufficient conditions described above. Finally, since each structure element corresponds to a single node in layer, given a collection of the structure elements obtained by Algorithm 1 we concatenate them altogether to form our topological layer.

Definition 3.1 (Topological layer (TopLayer) based on weighted persistent landscapes). For $n_h \in \mathbb{N}$, let $\boldsymbol{\eta}_i = (\theta_i, \omega_i)$ denote the set of parameters for the i -th element and $\boldsymbol{\eta} = (\boldsymbol{\eta}_i)_{i=1}^{n_h}$. Given \mathcal{D} and resolution ν , we define our topological layer by a parametrized mapping

with $\boldsymbol{\eta}$ of $\mathbb{D} \rightarrow \mathbb{R}^{n_h}$ such that

$$\mathcal{D} \mapsto (S_{\boldsymbol{\eta}_i}(\mathcal{D}; \nu))_{i=1}^{n_h}. \quad (6)$$

Note that this is nothing but a concatenation of n_h topological structure elements (nodes) with different parameter sets (thus n_h is our layer dimension). The topological layer defined above is trainable via backpropagation as each $S_{\boldsymbol{\eta}_i}$ is differentiable with respect to $\boldsymbol{\eta}_i$. Figure 1 provides some real data examples of persistent landscapes for 1-dimensional features. As shown in Figure 2, topological features are expected to be robust against external noise.

4 Differentiability

This section is devoted to the analysis of the differential behavior of the proposed topological layer with respect to its inputs (or outputs from previous layer), by computing the derivatives $\frac{\partial h_{top}}{\partial X}$. Since $\frac{\partial h_{top}}{\partial X} = \frac{\partial h_{top}}{\partial \mathcal{D}_X} \circ \frac{\partial \mathcal{D}_X}{\partial X}$, this can be done by combining two derivatives $\frac{\partial \mathcal{D}_X}{\partial X}$ and $\frac{\partial h_{top}}{\partial \mathcal{D}_X}$. We have extended Poulenard et al. (2018) so that we can compute above derivatives for general persistent homology under arbitrary filtration in our setting. We present the result in Theorem 4.1.

Theorem 4.1. *Let f be the filtration function. Let ξ be a map from each birth-death point $(b_i, d_i) \in \mathcal{D}_X$ to a pair of simplices (β_i, δ_i) . Suppose that ξ is locally constant at X , $f(\beta_i)$ and $f(\delta_i)$ are differentiable with respect to X_j 's, and $g_{\boldsymbol{\theta}}$ is differentiable. Then, h_{top} is differentiable and*

$$\begin{aligned} \frac{\partial h_{top}}{\partial X_j} &= \sum_i \frac{\partial f(\beta_i)}{\partial X_j} \sum_{l=1}^m \frac{\partial g_{\boldsymbol{\theta}}}{\partial x_l} \sum_{k=1}^{K_{\max}} \omega_k \frac{\partial \lambda_k(lv)}{\partial b_i} \\ &+ \sum_i \frac{\partial f(\delta_i)}{\partial X_j} \sum_{l=1}^m \frac{\partial g_{\boldsymbol{\theta}}}{\partial x_l} \sum_{k=1}^{K_{\max}} \omega_k \frac{\partial \lambda_k(lv)}{\partial d_i}. \end{aligned}$$

Proof. Let K be the simplicial complex, and suppose all the simplices are ordered in the filtration so that the values of f are nondecreasing, i.e. if ς comes earlier than τ then $f(\varsigma) \leq f(\tau)$. Note that the map ξ from each birth-death point $(b_i, d_i) \in \mathcal{D}_X$ to a pair of simplices (β_i, δ_i) is simply the pairing returned by the standard persistence diagram (Carlsson et al., 2005). Let γ be the homological feature corresponding to (b_i, d_i) , then the birth simplex β_i is the simplex that forms γ in $K_{b_i} = f^{-1}(-\infty, b_i]$, and the death simplex δ_i is the simplex that causes γ to collapse in $K_{d_i} = f^{-1}(-\infty, d_i]$. For example, if γ were to be a 1-dimensional feature, then β_i is the edge in K_{b_i} that forms the loop corresponding to γ , and δ_i is the triangle in K_{d_i} which incurs the loop corresponding to γ can be contracted in K_{d_i} .

Now, $f(\xi(b_i)) = f(\beta_i) = b_i$ and $f(\xi(d_i)) = f(\delta_i) = d_i$, and from ξ being locally constant on X ,

$$\frac{\partial b_i}{\partial X_j} = \frac{\partial f(\xi(b_i))}{\partial X_j} = \frac{\partial f(\beta_i)}{\partial X_j}, \quad \frac{\partial d_i}{\partial X_j} = \frac{\partial f(\xi(d_i))}{\partial X_j} = \frac{\partial f(\delta_i)}{\partial X_j}. \quad (7)$$

Therefore, the derivatives of the birth value and the death value are the derivatives of the filtration function evaluated at the corresponding pair of simplices. And $\frac{\partial \mathcal{D}_X}{\partial X}$ is the collection of these derivatives, hence applying (18) gives

$$\frac{\partial \mathcal{D}_X}{\partial X} = \left\{ \left(\frac{\partial b_i}{\partial X_j}, \frac{\partial d_i}{\partial X_j} \right) \right\}_{(b_i, d_i) \in \mathcal{D}_X, X_j \in X} = \left\{ \left(\frac{\partial f(\beta_i)}{\partial X_j}, \frac{\partial f(\delta_i)}{\partial X_j} \right) \right\}_{\xi^{-1}(\beta_i, \delta_i) \in \mathcal{D}_X, X_j \in X}. \quad (8)$$

For computing $\frac{\partial h_{top}}{\partial \mathcal{D}_X}$, note that $\frac{\partial h_{top}}{\partial b_i}$ can be computed using chain rule as

$$\begin{aligned} \frac{\partial h_{top}}{\partial b_i} &= \frac{\partial S_{\theta, \omega}}{\partial b_i} = \frac{\partial (g_{\theta} \circ \bar{\Lambda}_{\omega})}{\partial b_i} = \nabla g_{\theta} \circ \frac{\partial \bar{\Lambda}_{\omega}}{\partial b_i} \\ &= \sum_{l=1}^m \frac{\partial g_{\theta}}{\partial x_l} \frac{\partial \bar{\lambda}_{\omega}(l\nu)}{\partial b_i}, \end{aligned}$$

where we use x_l as shorthand notation for input of the function g_{θ} . Then, applying $\bar{\lambda}_{\omega}(l\nu) = \sum_{k=1}^{K_{max}} \omega_k \lambda_k(l\nu)$ gives

$$\frac{\partial h_{top}}{\partial b_i} = \sum_{l=1}^m \frac{\partial g_{\theta}}{\partial x_l} \sum_{k=1}^{K_{max}} \omega_k \frac{\partial \lambda_k(l\nu)}{\partial b_i}. \quad (9)$$

Similarly,

$$\frac{\partial h_{top}}{\partial d_i} = \sum_{l=1}^m \frac{\partial g_{\theta}}{\partial x_l} \sum_{k=1}^{K_{max}} \omega_k \frac{\partial \lambda_k(l\nu)}{\partial d_i}. \quad (10)$$

And therefore, $\frac{\partial h_{top}}{\partial \mathcal{D}_X}$ is the collection of these derivatives, i.e.,

$$\frac{\partial h_{top}}{\partial \mathcal{D}_X} = \left\{ \left(\sum_{l=1}^m \frac{\partial g_{\theta}}{\partial x_l} \sum_{k=1}^{K_{max}} \omega_k \frac{\partial \lambda_k(l\nu)}{\partial b_i}, \sum_{l=1}^m \frac{\partial g_{\theta}}{\partial x_l} \sum_{k=1}^{K_{max}} \omega_k \frac{\partial \lambda_k(l\nu)}{\partial d_i} \right) \right\}_{(b_i, d_i) \in \mathcal{D}_X}. \quad (11)$$

Hence, by combining (19) and (22), $\frac{\partial h_{top}}{\partial X}$ can be computed as

$$\begin{aligned} \frac{\partial h_{top}}{\partial X_j} &= \sum_i \frac{\partial h_{top}}{\partial b_i} \frac{\partial b_i}{\partial X_j} + \sum_i \frac{\partial h_{top}}{\partial d_i} \frac{\partial d_i}{\partial X_j} \\ &= \sum_i \frac{\partial f(\beta_i)}{\partial X_j} \sum_{l=1}^m \frac{\partial g_{\theta}}{\partial x_l} \sum_{k=1}^{K_{max}} \omega_k \frac{\partial \lambda_k(l\nu)}{\partial b_i} + \sum_i \frac{\partial f(\delta_i)}{\partial X_j} \sum_{l=1}^m \frac{\partial g_{\theta}}{\partial x_l} \sum_{k=1}^{K_{max}} \omega_k \frac{\partial \lambda_k(l\nu)}{\partial d_i}. \end{aligned}$$

□

Note that $\frac{\partial \lambda_k}{\partial b_i}, \frac{\partial \lambda_k}{\partial d_i}$ are nothing but piecewise constant functions and are easily computed even in explicit forms. Also $\frac{\partial g_{\theta}}{\partial x_l}$ can be easily realized by using an automatic differentiation

framework such as `tensorflow` or `pytorch`.

4.1 DTM function

Here we provide a specific example of computing $\frac{\partial f(\varsigma)}{\partial X_j}$ when f is the DTM filtration which has not been explored in previous approaches. We first consider the case of (4) where X_j 's are data points, as in Proposition 4.1. See Appendix C.2 for the proof.

Proposition 4.1. *When X_j 's and ς satisfy that $\sum_{X_i \in N_k(y)} \varpi_i \|X_i - y_l\|^r$ are different for each $y_l \in \varsigma$, then $f(\varsigma)$ is differentiable with respect to X_j and*

$$\frac{\partial f(\varsigma)}{\partial X_j} = \frac{\varpi'_j \|X_j - y\|^{r-2} (X_j - y) I(X_j \in N_k(y))}{\left(\hat{d}_{m_0}(y)\right)^{r-1} m_0 \sum_{i=1}^n \varpi_i},$$

where I is an indicator function and $y = \arg \max_{z \in \varsigma} \hat{d}_{m_0}(z)$. In particular, f is differentiable a.e. with respect to Lebesgue measure on X .

Similarly, we consider the case of (5) where X_j 's are weights, as in Proposition 4.2. See Appendix C.3 for the proof.

Proposition 4.2. *When X_j 's and ς satisfy that $\sum_{Y_i \in N_k(y)} X_i' \|Y_i - y_l\|^r$ are different for each $y_l \in \varsigma$, then $f(\varsigma)$ is differentiable with respect to X_j and*

$$\frac{\partial f(\varsigma)}{\partial X_j} = \frac{\|Y_j - y\|^r I(Y_j \in N_k(y)) - m_0 \left(\hat{d}_{m_0}(y)\right)^r}{r \left(\hat{d}_{m_0}(y)\right)^{r-1} m_0 \sum_{i=1}^n X_i},$$

where $y = \arg \max_{y \in \varsigma_i} \hat{d}_{m_0}(y)$. In particular, f is differentiable a.e. with respect to Lebesgue measure on X and Y .

Computation of $\frac{\partial h_{top}}{\partial \mu_i}$, $\frac{\partial h_{top}}{\partial \varsigma_i}$ are simpler and can be done in a similar fashion. In the experiments, we set $r = 2$.

5 Stability Analysis

A key property of the topological layer is stability; its discriminating power should remain stable against non-systematic noise or perturbation of input data. In this section, we shall provide our theoretical results on the stability properties of the proposed layer defined in (6). In what follows, we address the stability for each structure element with respect to change in persistent diagrams.

Theorem 5.1. *Given a Lipschitz function g_θ with Lipschitz constant L_g and resolution ν , for two persistent diagram $\mathcal{D}, \mathcal{D}'$,*

$$|S_{\theta, \omega}(\mathcal{D}; \nu) - S_{\theta, \omega}(\mathcal{D}'; \nu)| \leq L_g m^{1/2} d_B(\mathcal{D}, \mathcal{D}').$$

Proof of Theorem 5.1 is given in Appendix C.4. Theorem 5.1 shows that $S_{\theta, \omega}$ is stable with respect to the bottleneck distance (2.2). It should be noted that here our result only requires Lipschitz continuity of g_θ .

Next corollary shows that under certain conditions our approach may provide an improved bound compared to Hofer et al. (2017).

Corollary 5.1. *Let $n_{\mathcal{D}}$ denote the number of points in the persistent diagram \mathcal{D} . Then, the ratio of our stability bound in Theorem 5.1 to that in Hofer et al. (2017) is strictly upper bounded by*

$$\frac{C_{g_\theta, T, \nu}}{1 + C_{\mathcal{D}, \mathcal{D}'}(n_{\mathcal{D}} - 1)},$$

where $C_{g_\theta, T, \nu}, C_{\mathcal{D}, \mathcal{D}'}$ are constants to be specified in the proof.

See Appendix C.5 for the proof. Corollary 5.1 implies that our stability bound is tighter than that of Hofer et al. (2017) at polynomial rates. Hence for complex data structures where we would possibly get many birth-death pairs in each \mathcal{D} , our proposed layer guarantees tighter stability property.

In particular, for our DTM-function-based filtration using (4) or (5), Theorem 5.2 can be turned into the stability result with respect to the input X .

Theorem 5.2. *Suppose $r = 2$ is used for the DTM function. Let a differentiable function g_θ and resolution ν be given, and let P be a distribution. For the case when X_j 's are data points, i.e. when (4) is used as the DTM filtration of X , define P_n as the empirical distribution defined as $P_n = \frac{\sum_{i=1}^n \varpi_i \delta_{X_i}}{\sum_{i=1}^n \varpi_i}$. For the case when X_j 's are weights, i.e. when (5) is used as the DTM filtration of X , define P_n as the empirical distribution defined as $P_n = \frac{\sum_{i=1}^n X_i \delta_{Y_i}}{\sum_{i=1}^n X_i}$. Let \mathcal{D}_P be the persistence diagram of the DTM filtration of P , and \mathcal{D}_X be the persistence diagram of the DTM filtration of X , as in (4) when X_j 's are data points, or as in (5) when X_j 's are weights. Then,*

$$\begin{aligned} & |S_{\theta, \omega}(\mathcal{D}_X; \nu) - S_{\theta, \omega}(\mathcal{D}_P; \nu)| \\ & \leq L_g m^{1/2} m_0^{-1/2} W_2(P_n, P). \end{aligned}$$

See Section C.6 for the proof. Theorem 5.2 implies that if the empirical distribution P_n from our input X approximates the true distribution P well with respect to the Wasserstein distance $W_2(P_n, P)$, then our topological layers constructed on those observed points are

stable with respect to small perturbations of the Wasserstein distance. This means the topological information embedded in the proposed layer is robust against small noise, data corruption, or outliers.

We have also discussed the stability result for the Vietoris-Rips or the Čech complex in Section B.

6 Experiments

To demonstrate the effectiveness of the proposed approach, we study classification problems on three different datasets: MNIST handwritten digits, 3D object, and CIFAR-10. To fairly evaluate the benefits of using our proposed method, we keep the network architecture as simple as possible so that we can focus on benefits from our topological layer modules. Even though we do not have any restrictions on where to place the proposed layer, in the experiments we put our topological layer only at the beginning of the network to make a fair comparison with Hofer et al. (2017). In the experiments, we want to explore the benefits of our layer through the following questions: 1) does it make the network more robust and reliable against noise, etc.? and 2) does it improve the overall generalization capability compared to vanilla models? We intentionally use a small number of training data (~ 1000) so that the convergence rates could be included in the evaluation criteria. We refer to Appendix C.8 for details about each simulation and model architectures.

Robustness on MNIST handwritten digits

We first perform the classification task of images of handwritten digits using MNIST dataset. Each digit has its own distinctive topological information which can be encoded into the proposed topological layer as illustrated in Figure 1.

Topological layer. To compute persistent diagrams, we proceed with (5) where we define fixed 28×28 points on grid and use a set of grayscale values X as a weight vector for the fixed points with the smoothing parameter $m_0 = 0.1, r = 2$. Then we construct each structure element of our topological layer with $K_{\max} = 3, T = 0.5, m = 100$ by using the affine transformation described in Section 3.2. We use both 0- and 1-dimensional features.

Noise and corruption process. The *corruption process* is designed by a random omission of pixel values in the raw input; we randomly remove a certain percentage of signal pixels from each sample (so it has fewer data points). In the *noise process* we add a certain amount of uniformly-distributed noise signals over each example. The example of the corrupted and noisy image is illustrated in Figure 2.

Baselines & Simulation. As our baseline methods, we employ 2-layer vanilla MLP, 2-layer CNN, and the topological signature method by Hofer et al. (2017) (which we will

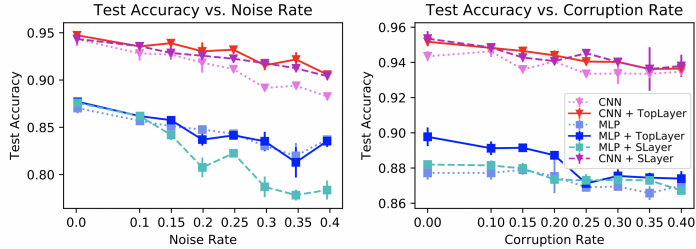


Figure 3: In MNIST experiment, adding TopLayer (ours) contributes to marginal improvement in accuracy and robustness to noise and corruption. In particular, we observe that the models augmented with the TopLayer are relatively less prone to noise. Error bars indicate standard deviation across different initializations.

Model	Test Accuracy
Vanilla MLP	0.755 ± 0.009
Deep Sets	0.937 ± 0.010
Hofer et al. (2017)	0.998 ± 0.001
PointNet	1.00 ± 0.00
Ours	0.993 ± 0.002

Table 1: In 3D shape classification, the proposed method achieves comparable accuracy to the state-of-the-art PointNet, even with a relatively small network complexity.



Figure 4: Eight distinct 3D geometries that completely characterize geometric structures on three-dimensional manifolds (Collins, 2004)

refer to as SLayer). For the SLayer and our proposed approach (TopLayer), we augment the vanilla MLP and CNN with the features learned from these topological methods. To observe the marginal benefit of robustness provided by our method with respect to noise and corruption, we compute the average test accuracy across various noise and corruption rate given to the training dataset.

Result. In Figure 3 we observe that although improvement in accuracy over baseline methods is somewhat marginal, in overall the proposed approach (TopLayer) is more robust to noise and corruption than the SLayer by Hofer et al. (2017) or plain MLP/CNN. Particularly in the presence of noise, the decrement remains small consistently for TopLayer whereas a steep drop is observed for the other baselines.

3D shape classification

In this experiment, we consider the problem of 3D object classification. Specifically, we consider eight 3D geometric shapes inspired by Thurston’s *geometrization conjecture*, as shown in Figure 4. Final data are represented in 3D point cloud with added noise (noise rate of 0.25). Detailed data generating process is described in Appendix C.8.

Topological layer. We put our raw input X on the predefined grid space X_g (where the grid consists of 50^3 equi-spaced points) such that $X \subseteq X_g$ and extend the DTM function to the complex as described in Section 3.1, (4). Other configurations and parameter setting remain the same as before. This time we only use 1- and 2-dimensional features as they are

turned out to be influential.

Baselines & Simulation. As baseline methods, we use 2-layer vanilla MLP, MLP augmented with the SLayer (Hofer et al. (2017)) just like in the previous experiment on MNIST, and PointNet(Qi et al. (2016)), which is the state-of-the-art deep neural network model for 3D point-cloud data. We also employ Deep Sets (Zaheer et al., 2017, Section 4.1.3) which is known to perform well on a point cloud set, where we use two permutation equivariant layers. We compare the test accuracy of the MLP augmented with our TopLayer against these baseline methods on the 3D object dataset.

Result. As shown in Table 1, our method achieves a comparable level of test accuracy to the state-of-the-art PointNet, even with a relatively small network complexity. Our method performs on par with Hofer et al. (2017), and slightly better than Deep Sets. It is worth noting the difference between our method and the well-known baselines; both PointNet and Deep Sets internally generate numerous features that are translation- and rotation-invariant based on specific rules, whereas we explicitly code such information as TDA features. From vanilla MLP, it is sufficient to add only a small number of additional nodes (~ 10) for the TopLayer to boost the accuracy significantly (from 75 % to 99 %).

CIFAR-10 dataset classification

Here we aim to implement the image classification with the CIFAR-10 dataset, where 32×32 images are grouped into 10 classes. We use grayscale images for this experiment.

Topological layer. We use two types of filtrations together for this dataset. First, we compute a filtration where we use 32×32 input values as weights of the DTM function as we did in the MNIST case. Secondly, to capture the minutiae we use a 2D-grid filtration where we compute the persistent homology of superlevel sets where we directly take the 32×32 input as 2D-function values.

Baselines & Simulation. Typically CIFAR-10 dataset is studied via variants of CNN as it delivers the best performance. We employ 4-layer CNN, and CNN + SLayer as our baseline. We proceeded with the noise and corruption rates of 0.15.

Result. Although the overall accuracy suffers from the small sample size and color deficiency, it is observed that when topological layers are augmented in the network it increases accuracy in general. The proposed layers yield roughly 5% improvement in accuracy that has not been reaped by CNN.

7 Discussion

In this study, we have presented a novel topological layer based on weighted persistent landscapes where we can exploit topological features effectively. For the DTM filtration, we

Model	Accuracy under Noise/Corruption
4-Layer CNN	0.447 ± 0.021
Hofer et al. (2017)	0.461 ± 0.005
Ours	0.495 ± 0.002

Table 2: Classification accuracy for CIFAR-10 dataset

guarantee differentiability of the proposed layer with respect to inputs on general persistent homology. Hence, our study provides the first general topological layer which can be placed anywhere in the deep learning network. We also present new stability theorems that verify the robustness and efficiency of our approach. It is worth noting that our analytical results are extended to silhouettes (Chazal et al., 2014b, 2015).

The results in this paper pave the way to various interesting future work as it has bridged the gap between modern TDA tools and deep learning. In a forthcoming applied paper, we prepare extensive experiments with more complex real-world datasets where we try silhouette-based layers as well. Furthermore, although it is intuitively appealing to place the topological layer in the beginning of the network as it directly exploits useful geometric features of input data structure, there may be situations that placing the proposed layer in the middle of the architecture is more beneficial. We will be exploring this issue as well.

References

- Anai, H., Chazal, F., Glisse, M., Ike, Y., Inakoshi, H., Tinarrage, R., and Umeda, Y. Dtm-based filtrations. In *35th International Symposium on Computational Geometry (SoCG 2019)*, 2019.
- Barannikov, S. A. The framed Morse complex and its invariants. In *Singularities and bifurcations*, volume 21 of *Adv. Soviet Math.*, pp. 93–115. Amer. Math. Soc., Providence, RI, 1994.
- Brown, K. A. and Knudson, K. P. Nonlinear statistics of human speech data. *International Journal of Bifurcation and Chaos*, 19(07):2307–2319, 2009.
- Bubenik, P. Statistical topological data analysis using persistence landscapes. *The Journal of Machine Learning Research*, 16(1):77–102, 2015.
- Bubenik, P. The persistence landscape and some of its properties. *arXiv preprint arXiv:1810.04963*, 2018.
- Bubenik, P. and Dłotko, P. A persistence landscapes toolbox for topological statistics. *Journal of Symbolic Computation*, 78:91–114, 2017.
- Carlsson, G. Topology and data. *Bulletin of the American Mathematical Society*, 46(2): 255–308, 2009.
- Carlsson, G. and Gabrielsson, R. B. Topological approaches to deep learning. 2018. URL <http://arxiv.org/abs/1811.01122>.
- Carlsson, G., Zomorodian, A., Collins, A., and Guibas, L. J. Persistence barcodes for shapes. *International Journal of Shape Modeling*, 11(02):149–187, 2005.
- Carrière, M., Chazal, F., Ike, Y., Lacombe, T., Royer, M., and Umeda, Y. PersLay: A Neural Network Layer for Persistence Diagrams and New Graph Topological Signatures. *arXiv e-prints*, art. arXiv:1904.09378, Apr 2019.
- Chazal, F. and Michel, B. An introduction to topological data analysis: fundamental and practical aspects for data scientists. *arXiv preprint arXiv:1710.04019*, 2017.
- Chazal, F., Cohen-Steiner, D., Glisse, M., Guibas, L. J., and Oudot, S. Y. Proximity of persistence modules and their diagrams. In *Proceedings of the twenty-fifth annual symposium on Computational geometry*, pp. 237–246. ACM, 2009.
- Chazal, F., Cohen-Steiner, D., and Mérigot, Q. Geometric inference for probability measures. *Foundations of Computational Mathematics*, 11(6):733–751, 2011.

- Chazal, F., De Silva, V., and Oudot, S. Persistence stability for geometric complexes. *Geometriae Dedicata*, 173(1):193–214, 2014a.
- Chazal, F., Fasy, B. T., Lecci, F., Rinaldo, A., and Wasserman, L. Stochastic convergence of persistence landscapes and silhouettes. In *Proceedings of the thirtieth annual symposium on Computational geometry*, pp. 474. ACM, 2014b.
- Chazal, F., Fasy, B., Lecci, F., Michel, B., Rinaldo, A., and Wasserman, L. Subsampling methods for persistent homology. In *International Conference on Machine Learning*, pp. 2143–2151, 2015.
- Chazal, F., Massart, P., Michel, B., et al. Rates of convergence for robust geometric inference. *Electronic journal of statistics*, 10(2):2243–2286, 2016a.
- Chazal, F., Oudot, S. Y., Glisse, M., and De Silva, V. *The Structure and Stability of Persistence Modules*. SpringerBriefs in Mathematics. Springer Verlag, 2016b. URL <https://hal.inria.fr/hal-01330678>.
- Chazal, F., Fasy, B., Lecci, F., Michel, B., Rinaldo, A., and Wasserman, L. Robust topological inference: distance to a measure and kernel distance. *J. Mach. Learn. Res.*, 18: Paper No. 159, 40, 2017. ISSN 1532-4435.
- Collins, G. The shapes of space. *Scientific American*, 291:94–103, 08 2004. doi: 10.1038/scientificamerican0704-94.
- Daniely, A., Frostig, R., and Singer, Y. Toward deeper understanding of neural networks: The power of initialization and a dual view on expressivity. In *Advances In Neural Information Processing Systems*, pp. 2253–2261, 2016.
- Edelsbrunner, H. and Harer, J. *Computational topology: an introduction*. American Mathematical Soc., 2010.
- Edelsbrunner, H., Letscher, D., and Zomorodian, A. Topological persistence and simplification. In *Proceedings 41st Annual Symposium on Foundations of Computer Science*, pp. 454–463. IEEE, 2000.
- Emrani, S., Gentimis, T., and Krim, H. Persistent homology of delay embeddings and its application to wheeze detection. *IEEE Signal Processing Letters*, 21(4):459–463, 2014.
- Fasy, B. T., Kim, J., Lecci, F., and Maria, C. Introduction to the r package tda. *arXiv preprint arXiv:1411.1830*, 2014.
- Gabrielsson, R. B., Nelson, B. J., Dwaraknath, A., Skraba, P., Guibas, L. J., and Carlsson, G. E. A topology layer for machine learning. *CoRR*, 2019. URL <http://arxiv.org/abs/1905.12200>.

- Gamble, J. and Heo, G. Exploring uses of persistent homology for statistical analysis of landmark-based shape data. *Journal of Multivariate Analysis*, 101(9):2184–2199, 2010.
- Ghrist, R. Barcodes: the persistent topology of data. *Bulletin of the American Mathematical Society*, 45(1):61–75, 2008.
- Guss, W. H. and Salakhutdinov, R. On characterizing the capacity of neural networks using algebraic topology. *arXiv preprint arXiv:1802.04443*, 2018.
- Hatcher, A. *Algebraic Topology*. Cambridge University Press, 2002.
- He, K., Zhang, X., Ren, S., and Sun, J. Deep residual learning for image recognition. In *Proceedings of the IEEE conference on computer vision and pattern recognition*, pp. 770–778, 2016.
- Hofer, C., Kwitt, R., Niethammer, M., and Uhl, A. Deep learning with topological signatures. In *Advances in Neural Information Processing Systems*, pp. 1634–1644, 2017.
- Hofer, C., Kwitt, R., Dixit, M., and Niethammer, M. Connectivity-optimized representation learning via persistent homology. *arXiv preprint arXiv:1906.09003*, 2019.
- Krizhevsky, A., Sutskever, I., and Hinton, G. E. Imagenet classification with deep convolutional neural networks. In *Advances in neural information processing systems*, pp. 1097–1105, 2012.
- LeCun, Y., Bottou, L., Bengio, Y., et al. Lenet-5, convolutional neural networks (2015). Retrieved June, 1, 2016.
- Liu, J.-Y., Jeng, S.-K., and Yang, Y.-H. Applying topological persistence in convolutional neural network for music audio signals. *arXiv preprint arXiv:1608.07373*, 2016.
- Nanda, V. and Sazdanović, R. Simplicial models and topological inference in biological systems. In *Discrete and topological models in molecular biology*, pp. 109–141. Springer, 2014.
- Pereira, C. M. and de Mello, R. F. Persistent homology for time series and spatial data clustering. *Expert Systems with Applications*, 42(15-16):6026–6038, 2015.
- Poulenard, A., Skraba, P., and Ovsjanikov, M. Topological function optimization for continuous shape matching. In *Computer Graphics Forum*, volume 37, pp. 13–25. Wiley Online Library, 2018.
- Qi, C. R., Su, H., Mo, K., and Guibas, L. J. Pointnet: Deep learning on point sets for 3d classification and segmentation. *arXiv preprint arXiv:1612.00593*, 2016.

- Raghu, M., Poole, B., Kleinberg, J., Ganguli, S., and Dickstein, J. S. On the expressive power of deep neural networks. In *Proceedings of the 34th International Conference on Machine Learning-Volume 70*, pp. 2847–2854. JMLR. org, 2017.
- Rieck, B., Togninalli, M., Bock, C., Moor, M., Horn, M., Gumbsch, T., and Borgwardt, K. Neural persistence: A complexity measure for deep neural networks using algebraic topology. *arXiv preprint arXiv:1812.09764*, 2018.
- Seversky, L. M., Davis, S., and Berger, M. On time-series topological data analysis: New data and opportunities. In *Proceedings of the IEEE Conference on Computer Vision and Pattern Recognition Workshops*, pp. 59–67, 2016.
- Simonyan, K. and Zisserman, A. Very deep convolutional networks for large-scale image recognition. *arXiv preprint arXiv:1409.1556*, 2014.
- Szegedy, C., Liu, W., Jia, Y., Sermanet, P., Reed, S., Anguelov, D., Erhan, D., Vanhoucke, V., and Rabinovich, A. Going deeper with convolutions. In *Proceedings of the IEEE conference on computer vision and pattern recognition*, pp. 1–9, 2015.
- Tralie, C. J. and Perea, J. A. (quasi) periodicity quantification in video data, using topology. *SIAM Journal on Imaging Sciences*, 11(2):1049–1077, 2018.
- Umeda, Y. Time series classification via topological data analysis. *Information and Media Technologies*, 12:228–239, 2017.
- Venkataraman, V., Ramamurthy, K. N., and Turaga, P. Persistent homology of attractors for action recognition. In *Image Processing (ICIP), 2016 IEEE International Conference on*, pp. 4150–4154. IEEE, 2016.
- Xu, X., Cisewski-Kehe, J., Green, S. B., and Nagai, D. Finding cosmic voids and filament loops using topological data analysis. *Astronomy and Computing*, 27:34, Apr 2019. doi: 10.1016/j.ascom.2019.02.003.
- Zaheer, M., Kottur, S., Ravanbakhsh, S., Póczos, B., Salakhutdinov, R. R., and Smola, A. J. Deep sets. In *Advances in Neural Information Processing Systems 30*, pp. 3391–3401. 2017.
- Zhu, X. Persistent homology: An introduction and a new text representation for natural language processing. In *IJCAI*, pp. 1953–1959, 2013.
- Zomorodian, A. and Carlsson, G. Computing persistent homology. *Discrete & Computational Geometry*, 33(2):249–274, 2005.

APPENDIX

A Simplicial complex

A simplicial complex can be seen as a high dimensional generalization of a graph. Given a set V , an *(abstract) simplicial complex* is a set K of finite subsets of V such that $\alpha \in K$ and $\beta \subset \alpha$ implies $\beta \in K$. Each set $\alpha \in K$ is called its *simplex*. The *dimension* of a simplex α is $\dim \alpha = \text{card} \alpha - 1$, and the dimension of the simplicial complex is the maximum dimension of any of its simplices. Note that a simplicial complex of dimension 1 is a graph.

When approximating the topology of the underlying space by observed samples, a common choice is the *Čech complex*, defined next. Below, for any $x \in \mathbb{X}$ and $r > 0$, we let $\mathbb{B}_{\mathbb{X}}(x, r)$ denote the closed ball centered at x and radius $r > 0$.

Definition A.1 (Čech complex). *Let $\mathcal{X} \subset \mathbb{X}$ be finite and $r > 0$. The (weighted) Čech complex is the simplicial complex*

$$\check{\text{Cech}}_{\mathcal{X}}^{\mathbb{X}}(r) := \{\sigma \subset \mathcal{X} : \cap_{x \in \sigma} \mathbb{B}_{\mathbb{X}}(x, r) \neq \emptyset\}, \quad (12)$$

The superscript \mathbb{X} will be dropped when understood from the context.

Another common choice is the *Vietoris-Rips complex*, also referred to as *Rips complex*, where simplexes are built based on pairwise distances among its vertices.

Definition A.2. *The Rips complex $R_{\mathcal{X}}(r)$ is the simplicial complex defined as*

$$R_{\mathcal{X}}(r) := \{\sigma \subset \mathcal{X} : d(x_i, x_j) < 2r, \forall x_i, x_j \in \sigma\}. \quad (13)$$

Note that the Čech complex and Rips complex have following interleaving inclusion relationship

$$\check{\text{Cech}}_{\mathcal{X}_n}(r) \subset R_{\mathcal{X}_n}(r) \subset \check{\text{Cech}}_{\mathcal{X}_n}(2r). \quad (14)$$

In particular, when \mathbb{X} is a Euclidean space, then the constant 2 can be tightened to $\sqrt{2}$:

$$\check{\text{Cech}}_{\mathcal{X}_n}(r) \subset R_{\mathcal{X}_n}(r) \subset \check{\text{Cech}}_{\mathcal{X}_n}(\sqrt{2}r). \quad (15)$$

B Stability for Vietoris-Rips and Čech filtration

When we use Vietoris-Rips or Čech filtration, our result can be turned into the stability result with respect to points in Euclidean space. Let $\mathbb{X}, \mathbb{Y} \subset \mathbb{R}^d$ be two bounded sets.

The next corollary re-states our stability theorem with respect to points in \mathbb{R}^d .

Corollary B.1. *Let X, Y be any ϵ -coverings of \mathbb{X}, \mathbb{Y} , and let $\mathcal{D}_X, \mathcal{D}_Y$ denote persistent diagrams induced from the Rips or Čech filtration on X, Y respectively. Then we have*

$$|S_{\theta, \omega}(\mathcal{D}_X; \nu) - S_{\theta, \omega}(\mathcal{D}_Y; \nu)| \leq 2L_g m^{1/2} (d_{GH}(\mathbb{X}, \mathbb{Y}) + 2\epsilon). \quad (16)$$

The proof is given in Appendix C.7. Corollary B.1 implies that if we assume our observed data points are sufficiently decent quality in the sense that $\epsilon \rightarrow 0$, then our topological layers constructed on those observed points are stable with respect to small perturbations of the true representation under proper persistent homologies. Here, ϵ could be interpreted as an uncertainty from incomplete sampling. This means the topological information embedded in the proposed layer is robust against small sampling noise or data corruption by missingness. Moreover, since Gromov-Hausdorff distance is upper bounded by Hausdorff distance, the result in Corollary B.1 also holds when we use $d_H(X, Y)$ in place of $d_{GH}(X, Y)$ in RHS of (16).

Remark 1. *In fact, when we have very dense data that have been well-sampled uniformly over the true representation so that $\epsilon \rightarrow 0$, our result converges to the following.*

$$|S_{\theta, \omega}(\mathcal{D}_{\mathbb{X}}; \nu) - S_{\theta, \omega}(\mathcal{D}_{\mathbb{Y}}; \nu)| \leq 2L_g \left(\frac{T}{\nu}\right)^{1/2} d_{GH}(\mathbb{X}, \mathbb{Y}). \quad (17)$$

C Proofs

C.1 Proof of Theorem 4.1

Let K be the simplicial complex, and suppose all the simplices are ordered in the filtration so that the values of f are nondecreasing, i.e. if ς comes earlier than τ then $f(\varsigma) \leq f(\tau)$. Note that the map ξ from each birth-death point $(b_i, d_i) \in \mathcal{D}_X$ to a pair of simplices (β_i, δ_i) is simply the pairing returned by the standard persistence diagram (Carlsson et al., 2005). Let γ be the homological feature corresponding to (b_i, d_i) , then the birth simplex β_i is the simplex that forms γ in $K_{b_i} = f^{-1}(-\infty, b_i]$, and the death simplex δ_i is the simplex that causes γ to collapse in $K_{d_i} = f^{-1}(-\infty, d_i]$. For example, if γ were to be a 1-dimensional feature, then β_i is the edge in K_{b_i} that forms the loop corresponding to γ , and δ_i is the triangle in K_{d_i} which incurs the loop corresponding to γ can be contracted in K_{d_i} .

Now, $f(\xi(b_i)) = f(\beta_i) = b_i$ and $f(\xi(d_i)) = f(\delta_i) = d_i$, and from ξ being locally constant on X ,

$$\frac{\partial b_i}{\partial X_j} = \frac{\partial f(\xi(b_i))}{\partial X_j} = \frac{\partial f(\beta_i)}{\partial X_j}, \quad \frac{\partial d_i}{\partial X_j} = \frac{\partial f(\xi(d_i))}{\partial X_j} = \frac{\partial f(\delta_i)}{\partial X_j}. \quad (18)$$

Therefore, the derivatives of the birth value and the death value are the derivatives of the filtration function evaluated at the corresponding pair of simplices. And $\frac{\partial \mathcal{D}_X}{\partial X}$ is the

collection of these derivatives, hence applying (18) gives

$$\frac{\partial \mathcal{D}_X}{\partial X} = \left\{ \left(\frac{\partial b_i}{\partial X_j}, \frac{\partial d_i}{\partial X_j} \right) \right\}_{(b_i, d_i) \in \mathcal{D}_X, X_j \in X} = \left\{ \left(\frac{\partial f(\beta_i)}{\partial X_j}, \frac{\partial f(\delta_i)}{\partial X_j} \right) \right\}_{\xi^{-1}(\beta_i, \delta_i) \in \mathcal{D}_X, X_j \in X}. \quad (19)$$

For computing $\frac{\partial h_{top}}{\partial \mathcal{D}_X}$, note that $\frac{\partial h_{top}}{\partial b_i}$ can be computed using chain rule as

$$\begin{aligned} \frac{\partial h_{top}}{\partial b_i} &= \frac{\partial S_{\theta, \omega}}{\partial b_i} = \frac{\partial (g_{\theta} \circ \bar{\Lambda}_{\omega})}{\partial b_i} = \nabla g_{\theta} \circ \frac{\partial \bar{\Lambda}_{\omega}}{\partial b_i} \\ &= \sum_{l=1}^m \frac{\partial g_{\theta}}{\partial x_l} \frac{\partial \bar{\lambda}_{\omega}(l\nu)}{\partial b_i}, \end{aligned}$$

where we use x_l as shorthand notation for input of the function g_{θ} . Then, applying $\bar{\lambda}_{\omega}(l\nu) = \sum_{k=1}^{K_{max}} \omega_k \lambda_k(l\nu)$ gives

$$\frac{\partial h_{top}}{\partial b_i} = \sum_{l=1}^m \frac{\partial g_{\theta}}{\partial x_l} \sum_{k=1}^{K_{max}} \omega_k \frac{\partial \lambda_k(l\nu)}{\partial b_i}. \quad (20)$$

Similarly,

$$\frac{\partial h_{top}}{\partial d_i} = \sum_{l=1}^m \frac{\partial g_{\theta}}{\partial x_l} \sum_{k=1}^{K_{max}} \omega_k \frac{\partial \lambda_k(l\nu)}{\partial d_i}. \quad (21)$$

And therefore, $\frac{\partial h_{top}}{\partial \mathcal{D}_X}$ is the collection of these derivatives, i.e.,

$$\frac{\partial h_{top}}{\partial \mathcal{D}_X} = \left\{ \left(\sum_{l=1}^m \frac{\partial g_{\theta}}{\partial x_l} \sum_{k=1}^{K_{max}} \omega_k \frac{\partial \lambda_k(l\nu)}{\partial b_i}, \sum_{l=1}^m \frac{\partial g_{\theta}}{\partial x_l} \sum_{k=1}^{K_{max}} \omega_k \frac{\partial \lambda_k(l\nu)}{\partial d_i} \right) \right\}_{(b_i, d_i) \in \mathcal{D}_X}. \quad (22)$$

Hence, by combining (19) and (22), $\frac{\partial h_{top}}{\partial X}$ can be computed as

$$\begin{aligned} \frac{\partial h_{top}}{\partial X_j} &= \sum_i \frac{\partial h_{top}}{\partial b_i} \frac{\partial b_i}{\partial X_j} + \sum_i \frac{\partial h_{top}}{\partial d_i} \frac{\partial d_i}{\partial X_j} \\ &= \sum_i \frac{\partial f(\beta_i)}{\partial X_j} \sum_{l=1}^m \frac{\partial g_{\theta}}{\partial x_l} \sum_{k=1}^{K_{max}} \omega_k \frac{\partial \lambda_k(l\nu)}{\partial b_i} + \sum_i \frac{\partial f(\delta_i)}{\partial X_j} \sum_{l=1}^m \frac{\partial g_{\theta}}{\partial x_l} \sum_{k=1}^{K_{max}} \omega_k \frac{\partial \lambda_k(l\nu)}{\partial d_i}. \end{aligned}$$

C.2 Proof of Proposition 4.1

From (4), note that for any $y \in \varsigma$, $\hat{d}_{m_0}(y)$ is expanded as

$$\hat{d}_{m_0}(y) = \left(\frac{\sum_{X_i \in N_k(x)} \varpi'_i \|X_i - y\|^r}{m_0 \sum_{i=1}^n \varpi_i} \right)^{1/r},$$

where k is such that $\sum_{X_i \in N_{k-1}(y)} \varpi_i < m_0 \sum_{i=1}^n \varpi_i \leq \sum_{X_i \in N_k(y)} \varpi_i$, and $\varpi'_i = \sum_{X_j \in N_k(x)} \varpi_j - m_0 \sum_{j=1}^n \varpi_j$ for one of X_i 's that is k -th nearest neighbor of y and $\varpi'_i = \varpi_i$ otherwise. Hence,

by letting $y = \arg \max_{z \in \varsigma} \hat{d}_{m_0}(z)$, then

$$f_X(\varsigma) = \hat{d}_{X, m_0}(y) = \left(\frac{\sum_{X_i \in N_k(y)} \varpi'_i \|X_i - y\|^r}{m_0 \sum_{i=1}^n \varpi_i} \right)^{1/r},$$

where the notations f_X and \hat{d}_{X, m_0} are to clarify the dependency of f on X . And from the condition, $\hat{d}_{m_0}(y) > \hat{d}_{m_0}(z)$ holds for all $z \in \varsigma$. Hence for sufficiently small $\epsilon > 0$ and for any $Z' = \{Z_1, \dots, Z_n\}$ with $\|Z_j - X_j\| < \epsilon$,

$$f_Z(\varsigma) = \hat{d}_{Z, m_0}(y) = \left(\frac{\sum_{X_i \in N_k(x)} \varpi'_i \|Z_i - y\|^r}{m_0 \sum_{i=1}^n \varpi_i} \right)^{1/r}.$$

Hence, the derivative of f with respect to X is calculated as

$$\begin{aligned} \frac{\partial f(\varsigma)}{\partial X_j} &= \left(\frac{\sum_{X_i \in N_k(y)} \varpi'_i \|X_i - y\|^r}{m_0 \sum_{i=1}^n \varpi_i} \right)^{\frac{1}{r}-1} \times \frac{\varpi'_j \|X_j - y\|^{r-2} (X_j - y) I(X_j \in N_k(y))}{m_0 \sum_{i=1}^n \varpi_i} \\ &= \frac{\varpi'_j \|X_j - y\|^{r-2} (X_j - y) I(X_j \in N_k(y))}{\left(\hat{d}_{m_0}(y) \right)^{r-1} m_0 \sum_{i=1}^n \varpi_i}. \end{aligned}$$

C.3 Proof of Proposition 4.2

From (5), note that for any $y \in \varsigma$, $\hat{d}_{m_0}(y)$ is expanded as

$$\hat{d}_{m_0}(y) = \left(\frac{\sum_{X_i \in N_k(y)} X'_i \|Y_i - y\|^r}{m_0 \sum_{i=1}^n X_i} \right)^{1/r},$$

where k is such that $\sum_{Y_i \in N_{k-1}(y)} X_i < m_0 \sum_{i=1}^n X_i \leq \sum_{Y_i \in N_k(y)} X_i$, and $X'_i = \sum_{X_j \in N_k(y)} X_j - m_0 \sum_{j=1}^n X_j$ for one of Y_i 's that is k -th nearest neighbor of y and $X'_i = X_i$ otherwise. Hence, by letting $y = \arg \max_{z \in \varsigma} \hat{d}_{m_0}(z)$, then

$$f_X(\varsigma) = \hat{d}_{X, m_0}(y) = \left(\frac{\sum_{X_i \in N_k(y)} X'_i \|Y_i - y\|^r}{m_0 \sum_{i=1}^n X_i} \right)^{1/r},$$

where the notations f_X and \hat{d}_{X, m_0} are to clarify the dependency of f on X . And from the condition, $\hat{d}_{m_0}(y) > \hat{d}_{m_0}(z)$ holds for all $z \in \varsigma$. Hence for sufficiently small $\epsilon > 0$ and for any $Z' = \{Z_1, \dots, Z_n\}$ with $\|Z_j - X_j\| < \epsilon$,

$$f_Z(\varsigma) = \hat{d}_{Z, m_0}(y) = \left(\frac{\sum_{X_i \in N_k(y)} Z'_i \|Y_i - y\|^r}{m_0 \sum_{i=1}^n Z_i} \right)^{1/r}.$$

Hence, the derivative of f with respect to X is calculated as

$$\begin{aligned}
& \frac{\partial f(\varsigma)}{\partial X_j} \\
&= \frac{1}{r} \left(\frac{\sum_{X_i \in N_k(y)} X_i' \|Y_i - y\|^r}{m_0 \sum_{i=1}^n X_i} \right)^{\frac{1}{r}-1} \frac{\|Y_j - y\|^r I(Y_j \in N_k(y)) (m_0 \sum_{i=1}^n X_i) - m_0 \left(\sum_{X_i \in N_k(y)} X_i' \|Y_i - y\|^r \right)}{(m_0 \sum_{i=1}^n X_i)^2} \\
&= \frac{\|Y_j - y\|^r I(Y_j \in N_k(y)) - m_0 \left(\hat{d}_{m_0}(y) \right)^r}{r \left(\hat{d}_{m_0}(y) \right)^{r-1} m_0 \sum_{i=1}^n X_i}.
\end{aligned}$$

C.4 Proof of Theorem 5.1

Let \mathcal{D} and \mathcal{D}' be two persistence diagrams and let λ and λ' be their persistence landscapes. All the quantities derived from \mathcal{D}' are denoted by a variable name with superscript $'$ hereafter (e.g., $\lambda'_k(t), \overline{\Lambda}'_\omega$). For $\forall k \in \mathbb{N}$ and $\forall t \in [0, T]$, by Theorem 13 in Bubenik (2015) we have

$$|\lambda_k(t) - \lambda'_k(t)| \leq d_B(\mathcal{D}, \mathcal{D}').$$

Hence it follows that

$$\begin{aligned}
|\overline{\lambda}_\omega(t) - \overline{\lambda}'_\omega(t)| &= \left| \frac{1}{\sum_k \omega_k} \sum_{k=1}^{K_{max}} \omega_k \lambda_k(t) - \frac{1}{\sum_k \omega_k} \sum_{k=1}^{K_{max}} \omega_k \lambda'_k(t) \right| \\
&\leq \frac{1}{\sum_k \omega_k} \sum_{k=1}^{K_{max}} \omega_k |\lambda_k(t) - \lambda'_k(t)| \\
&\leq \frac{d_B(\mathcal{D}, \mathcal{D}')}{\sum_k \omega_k} \sum_{k=1}^{K_{max}} \omega_k = d_B(\mathcal{D}, \mathcal{D}').
\end{aligned} \tag{23}$$

Next, from the Lipschitz condition of g ,

$$|g_\theta(\overline{\Lambda}_\omega) - g_\theta(\overline{\Lambda}'_\omega)| \leq L_g \|\overline{\Lambda}_\omega - \overline{\Lambda}'_\omega\|_2.$$

Now in RHS, we have that

$$\begin{aligned}
\|\overline{\Lambda}_\omega - \overline{\Lambda}'_\omega\|_2 &\leq \left(m \sup_{t \in [0, T]} \left(\overline{\lambda}_\omega(t) - \overline{\lambda}'_\omega(t) \right)^2 \right)^{1/2} \\
&\leq (m \cdot d_B^2(\mathcal{D}, \mathcal{D}'))^{1/2} \\
&= m^{1/2} d_B(\mathcal{D}, \mathcal{D}'),
\end{aligned}$$

where the first inequality follows by definition and the second by $|\overline{\lambda}_\omega(t) - \overline{\lambda}'_\omega(t)| \leq d_B(\mathcal{D}, \mathcal{D}')$ for $\forall t \in [0, T]$ as shown in (23). Hence, the result follows.

C.5 Proof of Corollary 5.1

First note that the result of Hofer et al. (2017) used W_1 Wasserstein distance with L_r norm for $\forall r \in \mathbb{N}$, which will be denoted by $W_1^{L_r}$ in this proof. That is,

$$W_1^{L_r}(\mathcal{D}, \mathcal{D}') := \inf_{\gamma} \sum_{p \in \mathcal{D}_X} \|p - \gamma(p)\|_r$$

where γ ranges over all bijections $\mathcal{D} \rightarrow \mathcal{D}'$ (i.e., $W_1^{L_\infty}$ corresponds to W_1 in our definition 2.2).

Now we assume \mathcal{D} has at least two points. We consider a bijection γ^* that realizes the Wasserstein distance between \mathcal{D} and \mathcal{D}' : i.e. $\gamma^* = \operatorname{arginf}_{\gamma} \sum_{p \in \mathcal{D}} \|p - \gamma(p)\|_\infty$. Then we have that

$$d_B(\mathcal{D}, \mathcal{D}') \leq \sup_{p \in \mathcal{D}} \|p - \gamma^*(p)\|_\infty. \quad (24)$$

Now it immediately follows that

$$\begin{aligned} \sup_{p \in \mathcal{D}} \|p - \gamma^*(p)\|_\infty &\leq \sup_{p \in \mathcal{D}} \|p - \gamma^*(p)\|_r \\ &< \sum_{p \in \mathcal{D}} \|p - \gamma^*(p)\|_r \\ &= W_1^{L_r}(\mathcal{D}, \mathcal{D}'), \end{aligned} \quad (25)$$

which confirms $d_B(\mathcal{D}, \mathcal{D}')$ is always strictly less than $W_1^{L_r}(\mathcal{D}, \mathcal{D}')$ for all r .

On the other hand, if we let $p^* = \operatorname{argsup}_{p \in \mathcal{D}} \|p - \gamma^*(p)\|_r$, we have

$$\sum_{p \in \mathcal{D}} \|p - \gamma^*(p)\|_r = \sup_{p \in \mathcal{D}} \|p - \gamma^*(p)\|_r + \sum_{p \neq p^*} \|p - \gamma^*(p)\|_r.$$

And, it is easy to infer that

$$\begin{aligned} \sup_{p \in \mathcal{D}} \|p - \gamma^*(p)\|_\infty &\leq \sup_{p \in \mathcal{D}} \|p - \gamma^*(p)\|_\infty + (n_{\mathcal{D}} - 1) \inf_{p \in \mathcal{D}} \|p - \gamma^*(p)\|_\infty \\ &\leq \sup_{p \in \mathcal{D}} \|p - \gamma^*(p)\|_\infty + \sum_{p \neq p^*} \|p - \gamma^*(p)\|_\infty \\ &\leq \sup_{p \in \mathcal{D}} \|p - \gamma^*(p)\|_r + \sum_{p \neq p^*} \|p - \gamma^*(p)\|_r = W_1^{L_r}(\mathcal{D}, \mathcal{D}'). \end{aligned} \quad (26)$$

Now, let c_K denote the Lipschitz constant in Hofer et al. (2017, Theorem 1) and $c_{g_\theta, T, \nu}$ denote the constant term in our result in Theorem 5.1, i.e. $c_{g_\theta, T, \nu} = L_g \left(\frac{T}{\nu}\right)^{1/2}$. We want to upper bound the ratio $\frac{c_{g_\theta, T, \nu} d_B(\mathcal{D}, \mathcal{D}')}{c_K W_1^{L_r}(\mathcal{D}, \mathcal{D}')}$. By (24, 25, 26), this can be done as follows.

$$\begin{aligned}
\frac{c_{g_{\theta}, T, \nu} d_B(\mathcal{D}, \mathcal{D}')}{c_K W_1^{Lr}(\mathcal{D}, \mathcal{D}')} &< \frac{c_{g_{\theta}, T, \nu}}{c_K} \frac{\sup_{p \in \mathcal{D}} \|p - \gamma^*(p)\|_{\infty}}{\sup_{p \in \mathcal{D}} \|p - \gamma^*(p)\|_{\infty} + (n_{\mathcal{D}} - 1) \inf_{p \in \mathcal{D}} \|p - \gamma^*(p)\|_{\infty}} \\
&= \frac{c_{g_{\theta}, T, \nu}}{c_K} \frac{1}{1 + (n_{\mathcal{D}} - 1) \frac{\inf_{p \in \mathcal{D}} \|p - \gamma^*(p)\|_{\infty}}{\sup_{p \in \mathcal{D}} \|p - \gamma^*(p)\|_{\infty}}}.
\end{aligned}$$

Finally, we define $C_{g_{\theta}, T, \nu} := \frac{c_{g_{\theta}, T, \nu}}{c_K}$, $C_{\mathcal{D}, \mathcal{D}'} := \frac{\inf_{p \in \mathcal{D}} \|p - \gamma^*(p)\|_{\infty}}{\sup_{p \in \mathcal{D}} \|p - \gamma^*(p)\|_{\infty}}$, and the result follows.

It should be noted that the bound is actually very loose. However, we can still conclude that our bound is tighter than that of Hofer et al. (2017) at polynomial rates.

C.6 Proof of Theorem 5.2

Theorem 5.1 implies that

$$|S_{\theta, \omega}(\mathcal{D}_X; \nu) - S_{\theta, \omega}(\mathcal{D}_P; \nu)| \leq L_g m^{1/2} d_B(\mathcal{D}_X, \mathcal{D}_P). \quad (27)$$

Then, by stability theorem of persistent homology,

$$d_B(\mathcal{D}_X, \mathcal{D}_P) \leq \|d_{P_n, m_0} - d_{P, m_0}\|_{\infty}. \quad (28)$$

Also, from $r = 2$ in the DTM function, Theorem 3.5 from Chazal et al. (2011) gives

$$\|d_{P_n, m_0} - d_{P, m_0}\|_{\infty} \leq m_0^{-1/2} W_2(P_n, P). \quad (29)$$

Hence, combining (27), (28), and (29) altogether gives

$$|S_{\theta, \omega}(\mathcal{D}_X; \nu) - S_{\theta, \omega}(\mathcal{D}_P; \nu)| \leq L_g m^{1/2} m_0^{-1/2} W_2(P_n, P).$$

C.7 Proof of Corollary B.1

By Theorem 5.1, it suffices to show

$$d_B(\mathcal{D}_X, \mathcal{D}_Y) < 2(d_{GH}(\mathbb{X}, \mathbb{Y}) + 2\epsilon).$$

First note that since \mathbb{X}, \mathbb{Y} are bounded in Euclidean space, they are totally bounded metric spaces. Thus by Theorem 5.2 in Chazal et al. (2014a), we have

$$d_B(\mathcal{D}_{\mathbb{X}}, \mathcal{D}_{\mathbb{Y}}) \leq 2d_{GH}(\mathbb{X}, \mathbb{Y}).$$

Then, we find an upper bound of $d_B(\mathcal{D}_X, \mathcal{D}_Y)$ as

$$\begin{aligned}
d_B(\mathcal{D}_X, \mathcal{D}_Y) &\leq d_B(\mathcal{D}_X, \mathcal{D}_{\mathbb{X}}) + d_B(\mathcal{D}_{\mathbb{X}}, \mathcal{D}_{\mathbb{Y}}) + d_B(\mathcal{D}_{\mathbb{Y}}, \mathcal{D}_Y) \\
&\leq 2(d_{GH}(X, \mathbb{X}) + d_{GH}(\mathbb{X}, \mathbb{Y}) + d_{GH}(\mathbb{Y}, Y)) \\
&\leq 2(d_H(X, \mathbb{X}) + d_{GH}(\mathbb{X}, \mathbb{Y}) + d_H(\mathbb{Y}, Y)) \\
&< 2d_{GH}(\mathbb{X}, \mathbb{Y}) + 4\epsilon,
\end{aligned}$$

where the first inequality follows by triangle inequality, the second by Theorem 5.2 in Chazal et al. (2014a), the third by the fact that d_{GH} is upper bounded by d_H , and the last by the assumption that X, Y are ϵ -coverings of \mathbb{X}, \mathbb{Y} . Now, the results follows.

C.8 Experiment Details.

All the experiments were implemented using `Tensorflow` package in R along with TDA package Fasy et al. (2014) in R. We use mean and standard deviation across five runs of simulations with different network initializations. We remark that the basic purpose of our experiment design is to highlight the prospects and possibilities of using topological layer, not to win state-of-the-art performances.

C.8.1 MNIST dataset.

Raw input data was a 784 dimensional vector (reshaped from 28 by 28) of real values, each value being the pixel intensity. We use 16 nodes in the proposed topological layer. We use 1000 random samples for the training set, another non-overlapped 5000 random samples for the test set.

Models were designed to have simple structure for quick comparisons:

- Vanilla MLP: one hidden layer with 64 units with ReLU activations.
- CNN: two convolution layers followed by two fully connected layers. Dropout was used in training time with probability of 0.5.
- Hofer et al. (2017): 16 topological signature units were concatenated to the raw input to the Vanilla MLP structure. We used the value $\nu = 0.1$ for the hyperparameter.

Cross-entropy loss was used to train the network for 100 epochs, using Adam optimizer with mini-batches of size 32. Learning rates were 0.0001 for CNN, Hofer et al. (2017), ours, and MLP.

C.8.2 3D shape dataset.

Data generating process. First, the surface of each object is represented mathematically, followed by zero-centering and normalization so that maximum length (diameter) of any object is approximately equal to one. Then we randomly sample ~ 100 points uniformly over the surface of each object. Hence, it can be regarded as inhomogeneous point-cloud display without colors. Then we add spatial noise around the object as before (25% of noise added). As our sample is naturally corrupted, we do not consider the corruption process here. We use 1200 samples (150 per each class) for the training set, and 800 samples (100 per each class) for the test set.

Raw input data was a $B \times 3$ dimensional vector (B being the number of points sampled from the surface of the 3D object, 3 coordinate values for each points).

- Vanilla MLP, Hofer et al. (2017): We used the same configuration as in the MNIST case as above.
- Deep Sets (Zaheer et al., 2017): We use similar setting described in the point-cloud classification experiment by Zaheer et al. (2017) where use two permutation equivariant layers with dropout rate 0.5.

C.8.3 CIFAR-10 dataset.

All the images are 32×32 grayscale, normalized to 0-1 scale. 2 convolutional layers are placed, each of which followed by max-pooling layers and fully-connected layers. Each convolutional layer consists of 36 5×5 filters followed by 2×2 max-pooling filters. We use 1000 random samples for the training set, and another 2500 samples for the test set.